

# Galaxy And Mass Assembly (GAMA): detection of low-surface-brightness galaxies from SDSS data

Richard P. Williams,<sup>1</sup> I. K. Baldry,<sup>1\*</sup> L. S. Kelvin,<sup>1</sup> P. A. James,<sup>1</sup> S. P. Driver,<sup>2,3</sup>  
M. Prescott,<sup>4</sup> S. Brough,<sup>5</sup> M. J. I. Brown,<sup>6</sup> L. J. M. Davies,<sup>2</sup> B. W. Holwerda,<sup>7</sup>  
J. Liske,<sup>8</sup> P. Norberg,<sup>9</sup> A. J. Moffett<sup>2</sup> and A. H. Wright<sup>2</sup>

<sup>1</sup>*Astrophysics Research Institute, Liverpool John Moores University, IC2, Liverpool Science Park, 146 Brownlow Hill, Liverpool L3 5RF, UK*

<sup>2</sup>*International Centre for Radio Astronomy Research (ICRAR), University of Western Australia, Crawley, WA 6009, Australia*

<sup>3</sup>*Scottish Universities' Physics Alliance (SUPA), School of Physics and Astronomy, University of St Andrews, St Andrews KY16 9SS, UK*

<sup>4</sup>*Department of Physics and Astronomy, University of the Western Cape, Private Bag X17, Bellville 7535, South Africa*

<sup>5</sup>*Australian Astronomical Observatory, PO Box 915, North Ryde, NSW 1670, Australia*

<sup>6</sup>*School of Physics, Monash University, Clayton, VIC 3800, Australia*

<sup>7</sup>*University of Leiden, Sterrenwacht Leiden, Niels Bohrweg 2, NL-2333 CA Leiden, the Netherlands*

<sup>8</sup>*Hamburger Sternwarte, Universität Hamburg, Gojenbergsweg 112, D-21029 Hamburg, Germany*

<sup>9</sup>*CEA, Department of Physics, ICC, Durham University, South Road, Durham DH1 3LE, UK*

Accepted 2016 August 29. Received 2016 July 18; in original form 2016 April 1

## ABSTRACT

We report on a search for new low-surface-brightness galaxies (LSBGs) using Sloan Digital Sky Survey (SDSS) data within the Galaxy And Mass Assembly (GAMA) equatorial fields. The search method consisted of masking objects detected with SDSS PHOTO, combining *gri* images weighted to maximize the expected signal-to-noise ratio, and smoothing the images. The processed images were then run through a detection algorithm that finds all pixels above a set threshold and groups them based on their proximity to one another. The list of detections was cleaned of contaminants such as diffraction spikes and the faint wings of masked objects. From these, selecting potentially the brightest in terms of total flux, a list of 343 LSBGs was produced having been confirmed using VISTA Kilo-degree Infrared Galaxy Survey (VIKING) imaging. The photometry of this sample was refined using the deeper VIKING Z band as the aperture-defining band. Measuring their  $g - i$  and  $J - K$  colours shows that most are consistent with being at redshifts less than 0.2. The photometry is carried out using an AUTO aperture for each detection giving surface brightnesses of  $\mu_r \gtrsim 25$  mag arcsec<sup>-2</sup> and magnitudes of  $r > 19.8$  mag. None of these galaxies are bright enough to be within the GAMA main survey limit but could be part of future deeper surveys to measure the low-mass end of the galaxy stellar mass function.

**Key words:** techniques: image processing – galaxies: dwarf – galaxies: photometry.

## 1 INTRODUCTION

Most galaxy surveys to date have been limited by a combination of apparent magnitude and surface-brightness (SB) constraints. This has led to an over-representation of luminous high-SB galaxies compared to a complete volume-limited sample (Cross & Driver 2002). Generally, flux-limited samples have been used to construct our picture of galaxy types, e.g. the Hubble tuning fork (Hubble 1926). However, the majority of galaxies are, in fact, low-luminosity or low-mass ‘dwarfs’ (Binggeli, Sandage & Tammann 1988; Karachentsev et al. 2004; Driver et al. 2005; Baldry et al. 2012). Whilst many are late-type spirals, they often do not fit neatly

into the ‘tuning fork’. Dwarf galaxies have, for example, been classified as: irregulars (Hubble 1926; de Vaucouleurs 1959), dwarf ellipticals (Shapley 1938), dwarf spheroidals (de Vaucouleurs & Ables 1968), blue compact dwarfs (Zwicky & Zwicky 1971), little blue spheroids (Kelvin et al. 2014a), blue diffuse dwarfs (James et al. 2015), and ultradiffuse galaxies (van Dokkum et al. 2015).<sup>1</sup>

<sup>1</sup> Note that we do not include ultracompact dwarfs (Phillipps et al. 2001) in this classification list. They typically have half-light radii closer to the values of globular clusters (Gilmore et al. 2007), and are most likely the central star-cluster remnants of larger galaxies (Jennings et al. 2015; Janz et al. 2016). As Kissler-Patig (2004) argued, they are ‘neither dwarf galaxies nor ultracompact’.

\* E-mail: i.baldry@ljmu.ac.uk

A cold dark matter ( $\Lambda$ CDM) simulations have been used to make predictions for the number density of low-mass galaxies. When compared to observations these simulations show a discrepancy, known as the substructure problem (Moore et al. 1999), which can be characterized in two distinct ways. The first is the so-called missing satellite problem: the deficiency of the number of observed satellites, around the Milky Way in particular, compared to the number of subhaloes predicted by models (Klypin et al. 1999; Moore et al. 1999). The second deals with the discrepancy between the predicted number of haloes and observed galaxies on a cosmological scale (e.g. Peebles 2001).

There has been progress towards reducing the discrepancy between simulations and observations in the Local Group with the discovery of many faint dwarf galaxies around the Milky Way (Gilmore et al. 2007; Irwin et al. 2007; Walsh, Jerjen & Willman 2007; Belokurov et al. 2010) and M31 (Ibata et al. 2007; Martin et al. 2009; Richardson et al. 2011; Martin et al. 2013). Furthermore, the number of galaxies in simulations can be reduced by, for example, changing CDM to warm dark matter (Kang, Macciò & Dutton 2013; Lapi & Danese 2015), or by suppression of dwarf galaxy formation from a photoionizing background (Benson et al. 2002; Somerville 2002).

Unlike their satellite counterparts, which have a more complex and turbulent formation history, field dwarf galaxies form and evolve in isolation. Despite processes such as supernova feedback (Ferrara & Tolstoy 2000) and heating from the cosmic ionizing background radiation (Hoeft et al. 2006), they generally have a larger cool gas fraction and higher star formation rate than those dwarfs that are gravitationally bound to a larger system. Instead of being stripped away, most of their gas can cool back into the system (Rosenbaum et al. 2009). Thus, the simulations and observations of low-mass field galaxies test a different regime to satellite galaxies.

There is currently a significant difference in the number density of low-mass systems ( $10^{6.5} M_{\odot} < M_{*} < 10^7 M_{\odot}$ ) between observations and simulations. For instance Guo et al. (2011), through the use of simulations, predicted a number density of  $0.1 \text{ Mpc}^{-3} \text{ dex}^{-1}$ . Currently the best observations put that number density at  $\sim 0.02 \text{ Mpc}^{-3} \text{ dex}^{-1}$  within this mass range, from Baldry et al. (2012) using the Galaxy And Mass Assembly (GAMA; Driver et al. 2009) survey. Therefore, observations must push to deeper magnitudes, and lower masses, in order to test whether observational SB limits are the reason, or part of the reason, for the discrepancy.

The detection of faint low-mass galaxies is challenging, dwarf systems have an intrinsically lower SB than their higher mass counterparts and so are more difficult to detect against the sky (Disney 1976; Disney & Phillipps 1983; Kormendy 1985; Baldry, Glazebrook & Driver 2008). A typical definition in the literature for low-surface-brightness galaxies (LSBGs) is to have a central SB of  $\mu_{\text{B}} \gtrsim 23 \text{ mag arcsec}^{-2}$  (McGaugh 1996; Impey & Bothun 1997). This SB makes them difficult to detect against the sky and leads to detection biases (Disney 1976). Finding LSBGs is thus key to accounting for, and characterizing, the dwarf galaxy populations of both satellites and isolated galaxies. A full accounting is needed to comprehensively test models of galaxy formation that include low-mass galaxies.

### 1.1 Searches for field dwarf galaxies

There are different environments to consider when searching for LSBGs and these environments can be broadly defined as: (i) nearby satellite galaxies within the Local Group (e.g. Koposov et al. 2008; Walsh, Willman & Jerjen 2009); (ii) satellites in external groups and

clusters (e.g. van Dokkum et al. 2015; Davies, Davies & Keenan 2016); and (iii) field galaxies away from luminous galaxies and clusters, or within a random cosmological volume. Compared to the Local Group, where stars can be resolved, and around luminous galaxies and in clusters, where deep imaging is more easily done and membership is more easily assigned, finding LSBGs in the field is more problematic. A large area of the sky needs to be covered in order to obtain a cosmologically representative sample. This means that a lower depth is obtained in the imaging compared with targeted cluster surveys given the same amount of observing time. In addition, redshifts need to be obtained for galaxies in order to assign distances (Blanton et al. 2005; Geller et al. 2012).

To improve detection of these systems, specialized algorithms can be used to find LSBGs in images from wide surveys such as the Sloan Digital Sky Survey (SDSS; York et al. 2000). Kniazev et al. (2004) used SDSS data to search for galaxies of large angular size recovering most of the LSBGs from the Impey et al. (1996) catalogue. Fainter features can be found by co-adding images paying careful attention to sky subtraction (Fliri & Trujillo 2016); and/or known galaxies can be masked out, meaning specialized algorithms can be applied to the images to search for fainter light from LSBGs that were not initially detected (Scaramella & Sabatini 2009). Similar techniques, including smoothing of masked images, can be used to search for low-SB tidal features (Miskolczi, Bomans & Dettmar 2011). James et al. (2015) used a search of the SDSS data to search for galaxies with similar morphology to Leo P (Giovannelli et al. 2013), which has embedded H II regions within a blue diffuse galaxy, and were able to detect  $\sim 100$  of these sources.

Star-forming (SF) dwarf galaxies dominate the field dwarf population (Geha et al. 2012). Therefore, they can be detected using radio H I surveys, such as the Arecibo Legacy Fast ALFA survey (ALFALFA; Giovanelli et al. 2005), because they typically have high H I to stellar mass ratios (Baldry et al. 2008; Huang et al. 2012). The searching of optical images is then eased considerably, by knowing where to look, for example: Trachternach et al. (2006) and Du et al. (2015) have confirmed many hundreds of new LSBGs based on their H I detections, mostly in the field; Sand et al. (2015) confirmed five new blue diffuse dwarf galaxies within 10 Mpc, associated with ‘high-velocity clouds’ found in ALFALFA data; and Tollerud et al. (2015), using a blind H I survey (Galactic Arecibo L-Band Feed Array-H I, Peek et al. 2011), were able to detect two more faint diffuse galaxies, again within 10 Mpc.

### 1.2 Aims of this analysis

The galaxy stellar mass function (GSMF) is a fundamental tool used in studying the demographics of galaxies (Bell et al. 2003; Baldry et al. 2008; Muzzin et al. 2013). It describes the number density of galaxies as a function of their mass within a volume of the Universe. The GAMA survey team has accurately described the GSMF down to  $M_{*} = 10^8 M_{\odot}$ . The current incarnation, however, is likely incomplete at masses below this due to SB limits (Baldry et al. 2012). As such, in order to push below this limit it is important to carry out a search of the SDSS DR7 data within the GAMA fields. SDSS data have been chosen for this work as this survey has already demonstrated its suitability for finding low-SB systems (Kniazev et al. 2004).

The GAMA survey has made significant progress towards uncovering and classifying the dwarf population. For instance, Baldry et al. (2012) showed that the most common type of galaxy in the Universe is likely SF dwarf galaxies rather than passive. Kelvin et al. (2014a,b) measured the contribution of ‘little blue spheroids’,

Sd spirals and irregulars to the low-mass and low-luminosity number densities. Mahajan et al. (2015) showed that SF dwarf galaxies formed a unimodal population using various photometric and derived properties. However, progress still needs to be made into the search for, and detection of, LSBGs within this survey to work towards completing the census of galaxies.

This search is complicated, and the method employed depends on the type of data that is provided and the nature of the objects being searched for. The distance range desired for the detection of LSBGs in this paper is around 10–100 Mpc, which places them beyond the range of the Local Group and volume (McConnachie 2012). The volume out to 100 Mpc over the GAMA equatorial fields is 18 000 Mpc<sup>3</sup>. This is more cosmologically representative than studies in the local volume (<10 Mpc) because of the larger volume and longer sightlines that cut through filaments and void-like regions. A specialized detection algorithm was developed to detect LSBGs, which are difficult to detect because of sky noise and artefacts.

This paper deals with the method for the creation and implementation of such a search algorithm to find these LSBGs within SDSS imaging, with comparisons to VISTA Kilo-degree Infrared Galaxy Survey (VIKING; Edge et al. 2013) imaging. This is being used to confirm or deny a detection as the VIKING Z band is  $\sim 1$  mag deeper than SDSS *r* band when compared to an average spectral energy distribution for a low-redshift galaxy (Driver et al. 2012). In future, we plan to focus on finding similar objects in VIKING and, eventually, Kilo-Degree Survey (KiDS; Kuijken 2011) images which have deeper limits in SB than SDSS. Initially this can be done using a standard method (e.g. Source Extractor), before using this information to create masks to then apply the methods described and tested in this paper.

The outline of the paper is as follows. In Section 2, the different survey data are described; Section 3 deals with the development and implementation of the image processing code; Section 4 describes the algorithm used to search the images to find the LSBGs hidden within; and Section 5 presents the results and catalogue. Summary and conclusions are presented in Section 6.

## 2 SURVEYS

The newly detected objects presented in this work were discovered using SDSS *gri* imaging within the limits of the three GAMA equatorial regions, G09, G12, and G15. For confirmation that these detections are galaxies, further visual confirmation was required. This was achieved through the use of deep VIKING Z-band data. The technical details of these surveys are described below.

### 2.1 GAMA

The GAMA survey is a wide-field spectroscopic survey that was undertaken to study cosmology, galaxy structure, and galaxy evolution at low redshift (Driver et al. 2011; Liske et al. 2015). Redshifts of galaxies were obtained using the AAOmega spectrograph on the Anglo-Australian Telescope (AAT; Sharp et al. 2006; Hopkins et al. 2013). Spectra have been obtained for 238 000 objects in five survey regions (G02, G09, G12, G15, and G23, which are fields centred at RA 2h, 9h, 12h, 14.5h, and 23h), with a limiting magnitude of  $r < 19.8$  for the main survey over four of the fields. The total survey area is 286 deg<sup>2</sup>. Independent imaging has been compiled from several other surveys whose footprints fall on the GAMA regions, covering wavelengths from the far-ultraviolet to the radio (Driver et al. 2016b).

This paper primarily uses data from the three equatorial regions G09, G12, and G15, due to coverage of these areas by SDSS and VIKING. The galaxy stellar masses used in this paper were calculated using the method outlined in Taylor et al. (2011) updated to include VIKING Z- and Y-band data, in addition to SDSS data, in the fitting procedure. For these, a cosmology with  $H_0 = 70 \text{ km s}^{-1} \text{ Mpc}^{-1}$ ,  $\Omega_{m,0} = 0.3$  and  $\Omega_{\Lambda,0} = 0.7$  was assumed. Note these stellar masses and redshifts from the GAMA survey are used to define comparison samples, none of the newly detected LSBGs described in this paper have spectroscopic redshifts.

### 2.2 Sloan Digital Sky Survey

The SDSS (York et al. 2000) has observed over 10 000 deg<sup>2</sup> of sky. The imaging was done using 30 2048 × 2048 CCDs and five filters *u*, *g*, *r*, *i*, and *z* (Fukugita et al. 1996). Almost all of its standard imaging data were released in Data Release 7 (Abazajian et al. 2009). This imaging was taken in ‘drift scan’ mode. Each part of the sky was exposed for about 55 s as the sky moves across the detector, which was read out at the same rate. This created long strips of images in the scan direction. These strips, one for each detector, were subsequently processed through the SDSS PHOTO pipeline (Stoughton et al. 2002) and divided into fields along the scan direction for convenience of use.

The data used in this work are the corrected images in the DR7 data base. All information stored in the images is presented in counts, which can be converted into the AB magnitude system by applying equations supplied by SDSS. These images are supplemented by various masks for each filter. A code supplied by SDSS is used to extract the type of mask desired by the user (Stoughton et al. 2002).<sup>2</sup>

### 2.3 VISTA VIKING

The Visible and Infrared Survey Telescope for Astronomy (VISTA; Emerson & Sutherland 2010) is a 4.1-m wide-field telescope. It is located on Paranal Observatory in Chile. One of the surveys this telescope is carrying out is the VIKING survey. This survey covers 1400 deg<sup>2</sup> in the near-infrared *Z*, *Y*, *J*, *H*, and *K* bands. The *Z* band, in particular, was used as a check for the detections due to its improved depth of imaging over the SDSS bands. Notably the VISTA *Z* band was taken in dark time, unlike typical *z*-band observations that are ‘competing’ with visible bands.

## 3 IMAGE PROCESSING

The reduced SDSS images were processed in order to specifically search for LSBGs that had been missed by the SDSS pipeline. The image processing can be separated into five distinct phases: (i) masking of image fields; (ii) alignment of images; (iii) weighting to maximize the expected signal-to-noise ratio (SNR); (iv) co-adding of *g*, *r*, and *i* image fields; and (v) smoothing of the final image products. These processes are described in the following paragraphs.

SDSS uses a drift scan mode to take images. This leads to long images spread across the sky with a width equivalent to that of the detector. For ease these images are split into ‘fields’ of 1489 pixels by 2048 pixels, equivalent to  $\sim 590 \text{ arcsec} \times 810 \text{ arcsec}$ . The 6424 fields that were used for target selection were selected from the

<sup>2</sup> The corrected image files start with prefix fpC. The mask files start with prefix fpM, and were read using READATLASIMAGES-v5\_4\_11.

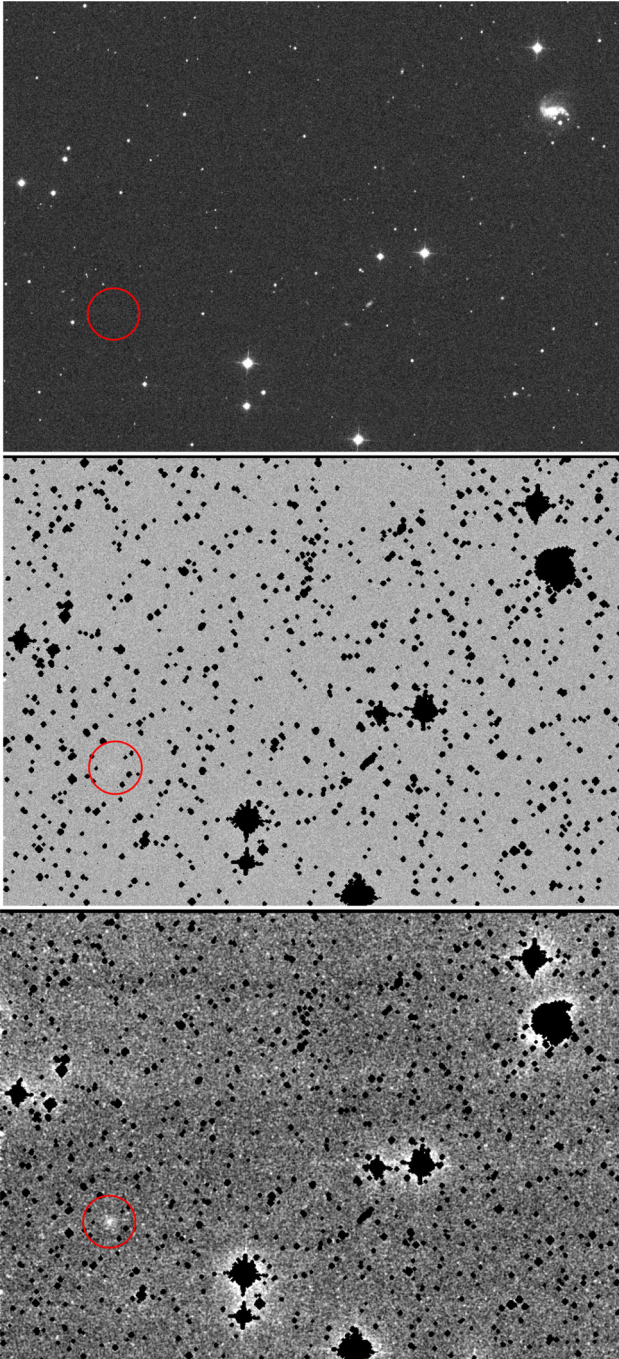


**Figure 1.** Panels showing how the images are affected by the processing described in Section 3. The top panel shows the initial image of an example field (run 1458, filter  $g$ , camera column 5, field 623). The middle panel shows the same field after masking of known sources detected from the SDSS PHOTO pipeline. The bottom panel shows the field after combining the  $g$ ,  $r$ , and  $i$  masked images and smoothing. This brings out the low-SB features around the brighter detected objects and gives a good representation of the challenges faced when trying to identify LSBGs. The red circle highlights the location at which an undetected LSBG becomes clearly visible after processing. The object is identified in the catalogue as LSB15283.

GAMA equatorial regions. An example of the image files taken from the SDSS is given in the top panel of Fig. 1.

The images were first masked to remove high-SB objects which have been discovered using SDSS PHOTO (Stoughton et al. 2002).

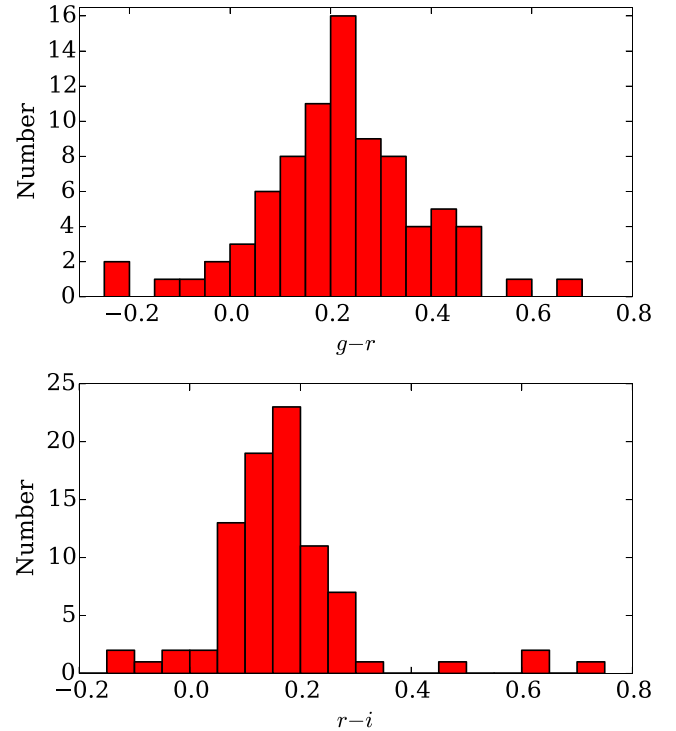


**Figure 2.** Histograms of the  $g - r$  colour of GAMA dwarf galaxies (top panel), with a median of 0.233, and of the  $r - i$  colour of the same galaxies (bottom panel), with a median of 0.154. The galaxies used for these plots fall in the stellar mass range  $10^6 M_{\odot} < M_{\star} < 10^{7.5} M_{\odot}$ .

Any pixel classed as being associated with a detected object was masked, including stars, galaxies, cosmic ray detections, and artefacts within the image fields. Note this is a pixel-based mask rather than a mask based on polygons or ellipses around detected objects, as shown in the middle panel of Fig. 1.

The data files taken from the SDSS for each field are not aligned with each other because the detectors from the different bands are not perfectly aligned in the cross-scan direction. The scan direction is in RA, for the equatorial fields, and the cross-scan direction is in Dec. The  $g$  and  $i$  images were aligned using a geometrical translation with the  $r$ -band coordinates as a reference, by up to 16 pixels difference ( $\approx 6.4$  arcsec) in the  $g$  band, and 5 pixels ( $\approx 2$  arcsec) in the  $i$  band. Once the alignment is complete all images are aligned to within 1 pixel ( $< 0.4$  arcsec). This remaining difference is not significant enough to be of concern because we are searching for significantly extended sources.

LSBGs are diffuse such that the noise in any flux measurement is dominated by the sky background (with standard deviation  $\sigma_{\text{sky}}$ ). In order to maximize the SNR in any co-added image, the images from each filter should therefore be weighted in proportion to  $S/\sigma_{\text{sky}}^2$ , where  $S$  is the expected signal level of a fiducial source. We are interested in optimizing for low-mass, SF dwarf galaxies. To do this, we determined the median colours of GAMA dwarf galaxies with  $10^6 M_{\odot} < M_{\star} < 10^{7.5} M_{\odot}$ . These values are  $g - r = 0.233$  and  $r - i = 0.154$  with the colour distributions shown in Fig. 2. The expected signals were then determined for a fiducial source with  $(g, r, i) = (19.387, 19.154, 19)$ , and using the equations provided by SDSS for each field. The ranges of counts are shown in Table 1.

**Table 1.** The filter, apparent magnitudes ( $m$ ) for a fiducial source, the range of signals ( $S$ ) calculated for different images, sky-noise values ( $\sigma_{\text{sky}}$ ), and weights ( $\omega$ ) to be applied to the images before co-adding.

| Filter | $m$    | Counts ( $S$ ) | $\sigma_{\text{sky}}$ | Weights ( $\omega$ ) |
|--------|--------|----------------|-----------------------|----------------------|
| $g$    | 19.387 | 4283–5148      | 4.37–6.55             | 1                    |
| $r$    | 19.154 | 4169–4770      | 5.29–6.41             | 0.558–0.921          |
| $i$    | 19.000 | 3245–4028      | 6.18–8.01             | 0.303–0.505          |

The  $\sigma_{\text{sky}}$  values were determined from the masked images, with the final weights relative to the  $g$  band given by

$$\omega = \frac{S/\sigma_{\text{sky}}^2}{S_g/\sigma_{\text{sky},g}^2} \quad (1)$$

The ranges in the final weights (Table 1) are a result of the different extinction and sky-noise conditions on the nights on which the respective fields were observed.

The final step is to smooth the images in order to further improve the SNR. SDSS use a maximum  $4 \times 4$  binning kernel for detection purposes, i.e. 16 pixels are co-added to increase the SNR. Here, we convolve an approximately circular kernel of diameter 7 pixels ( $\approx 3$  arcsec) with each image (in practice, the kernel is a  $7 \times 7$  matrix of ones and zeros, for inside and outside the circle, respectively). This diameter is chosen as at the larger distances of interest,  $\sim 100$  Mpc, we expect objects of only a few arcseconds on the sky (Impey & Bothun 1997). The bottom panel of Fig. 1 shows the effect that co-adding and smoothing has on the example image.

Now that the  $g$ ,  $r$ , and  $i$  bands for each field have been masked, weighted, co-added, and smoothed, using a larger kernel than was used by the PHOTO pipeline, there is increased sensitivity in the images for the discovery of field dwarf LSBGs than SDSS PHOTO was able to achieve. The next step is to develop an algorithm which can be used to detect these hitherto undetected galaxies.

#### 4 DETECTION ALGORITHM

For this analysis, we adopt  $5\sigma$  above the background of each processed image as the detection threshold. Neighbouring pixels with an  $\text{SNR} > 5$  are grouped into ‘candidate’ detections. For each candidate detection, we record the centroid position of the grouped pixels. This returned about one million candidate low-SB detections. These need to be processed to eliminate likely false detections, and to select potentially the brightest LSBGs in terms of total flux.

Most of candidate detections are from the excess light around bright stars and galaxies. This excess light is evident in the bottom panel of Fig. 1 for a typical field. In some fields there are also other artefacts. The list of sources therefore needs to be cleaned to remove these artefacts by applying a set of constraints to the detections list. These constraints are based on: (i) proximity to bright sources, (ii) anomalously high detection rates per field, and (iii) proximity to other candidate detections. The way these constraints are applied, and the reasons for applying them, is described in the following paragraphs.

In order to reject candidates that are caused by the unmasked light around bright sources, the percentages of masked pixels,  $\mathcal{P}_{50}$  and  $\mathcal{P}_{100}$ , within circles of radii 50 and 100 pixels around each candidate were determined (radii of  $\sim 20$  arcsec and 40 arcsec, respectively). The top panel of Fig. 3 shows histograms of  $\mathcal{P}_{50}$  and  $\mathcal{P}_{100}$  for the candidate detections; while the lower panel shows histograms for

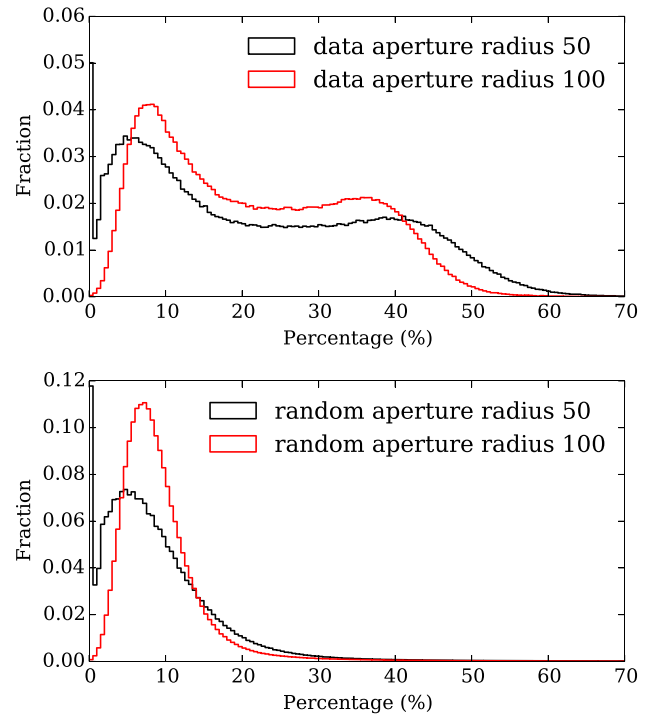


**Figure 3.** Histograms of the percentages of masked pixels,  $\mathcal{P}_{50}$  and  $\mathcal{P}_{100}$ , within apertures of radii 50 and 100 pixels placed around candidates (top panel) and around random positions (bottom panel). There is an obvious rise in the fraction of candidates that have a high percentage of masked pixels compared to randomly placed apertures. This is caused by low-SB emission around bright sources. Candidate detections falling within this second peak can be rejected with minimal impact on the effective search area.

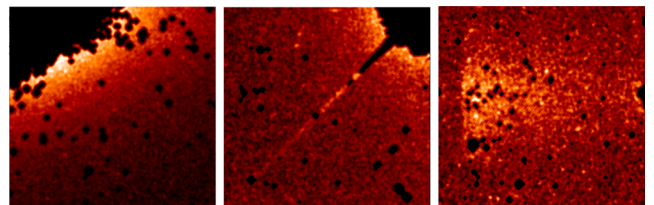


**Figure 4.** Examples of masked-and-smoothed images demonstrating some of the issues. The left-hand panel shows the faint wings of the light distribution of a large galaxy. The emission from the unmasked regions causes low-SB detections. The middle panel shows a diffraction spike; again the fainter areas of the spike are not masked. The right-hand panel shows an artefact caused by a bright star in a neighbouring field, giving a distinctive flat feature parallel to the edge of the image.

randomly placed apertures, with 1000 apertures each for  $\mathcal{P}_{50}$  and  $\mathcal{P}_{100}$  per field.

We would expect field LSBGs in terms of their proximity to bright sources, which are mostly stars, to behave more like the randomly placed apertures. We can see from the top panel of Fig. 3 that there is an extension to large  $\mathcal{P}$  values that is not evident for the randomly placed apertures. Therefore, we can reject candidates with large  $\mathcal{P}$  values while retaining the majority of genuine LSBGs. The criteria used for rejection were  $\mathcal{P}_{50} > 15$  per cent and  $\mathcal{P}_{100} > 15$  per cent. Applying this criteria to the random apertures results in 16 per cent of the random positions being rejected therefore this means that the effective search area is reduced to 84 per cent of the survey area.

Fig. 4 gives some examples of objects which were not removed by the masked-pixel checks carried out above, and which need to be

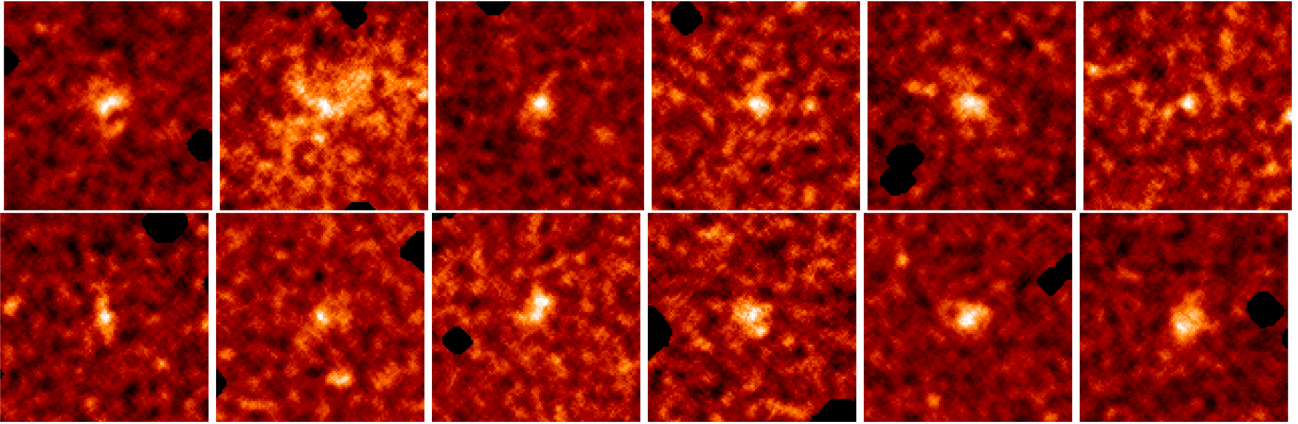


**Figure 5.** 12 confirmed LSBGs from the co-added, masked, and smoothed images created from SDSS  $g$ ,  $r$ , and  $i$  bands. Each candidate is positioned at the centre of the 35 arcsec  $\times$  35 arcsec images. The detections were confirmed by deeper VIKING Z-band observations.

dealt with as separate cases. The first of these are fields containing very extended wings of ultrabright objects, making the detection of LSBGs difficult as it produces a large number of erroneous LSBG detections within the images which need to be excluded. Therefore, the constraint decided on was to reject all fields with more than 100 candidate low-SB detections within it. This affects only 22 fields, which is a small enough number as to be easily visually checked, to ensure no obvious LSBGs were rejected.

A further issue is the detection of stray light from bright stars that are in a field adjacent to the detection. An example of this is in the right-hand image of Fig. 4. This shows that parts of the artefact have been masked with the effect of breaking the object up into several smaller detections. In order to try to remove these objects and others like it, a constraint is applied to the images whereby all candidates that have more than five other candidates within a radius of 120 arcsec are rejected. A random sample of these objects is visually inspected to ensure that predominantly artefacts are removed from the catalogue.

One of the main reasons for conducting this study is to check the completeness of the GAMA survey, i.e. detections with  $r < 19.8$  mag, or near to this limit, are of most interest. To select potentially bright LSBGs (in total flux), two apertures of diameter 10 and 15 arcsec are placed over the objects and the flux measured in both on the masked images. We select candidates whose flux was measured to be brighter than nominally 21.3 mag in one of the apertures for the final stage of analysis, and all others are rejected.

This reduces the number of candidates to about 5000 detections. This sample was visually inspected. The candidates were given an integer quality rank from 0 to 2 where: 0 means a false detection, a diffraction spike or other artefact; 1 means a possible LSBG detection, e.g. a small object in the smoothed images with no obvious extended structure; and 2 means a definite LSBG detection, an obvious extended source that had not been masked by SDSS. The number of possible and definite detections after this process was 652. All of the removed objects are artefacts like those depicted in Fig. 4.

The list of positions was finally visually checked against the same positions in the VIKING Z-band images, which were not used for detection. These VIKING images are deeper than SDSS images for galaxies. This final check, along with eliminating duplicates of the same object, produced a sample of 343 LSBGs. Fig. 5 shows examples of images that were visually checked and proven to be real. All of the objects with rank 2 were

confirmed by VIKING Z-band data, along with many of the rank 1 sources.<sup>3</sup>

## 5 RESULTS

### 5.1 Spatial distribution

The distribution of large-scale structure has been consistently shown to fall into filamentary structures within a  $\Lambda$ CDM universe, in both simulation and through observation (Press & Schechter 1974; Bahcall 1988; Alpaslan et al. 2014). It would be expected therefore that there would be some clustering of detections even for low-mass galaxies. As can be seen from Fig. 6, the newly detected LSBGs are consistent with being associated with the  $z < 0.1$  large-scale structures. However, this is stated cautiously as without accurate redshift information for these objects, it is not possible to state with certainty that they are connected to these structures.

### 5.2 Magnitudes

To select the potentially brightest LSBGs, we used fixed apertures applied to the co-added-masked SDSS images. These measurements are not ideal because of non-optimal apertures and potential sky-subtraction uncertainties. We compute automatic apertures from the deepest band, the VIKING Z band, and measure improved matched-aperture photometry in all the SDSS and VIKING bands. The magnitudes were calculated using a specially designed wrapper for Source Extractor (Bertin & Arnouts 1996) called IOTA. The code is described in Driver et al. (2016b) and is deployed in a similar way for this analysis.<sup>4</sup>

Magnitudes are calculated using two apertures, a fixed aperture with a diameter of 5 arcsec, and an AUTO aperture (Bertin & Arnouts 1996). The latter is used for the default magnitudes and colours, unless the AUTO aperture magnitude is fainter by more

<sup>3</sup> Note that 50 candidates had been assigned OBJIDs from the SDSS data base. This was a concern as it was believed that all detected objects had been masked out using the SDSS PHOTO pipeline output. However, upon inspection of the SDSS flags, it was found that the objects were not detected in enough of the bands to be considered as reliable detections. We therefore kept them in the sample of 343 new detections presented in this paper.

<sup>4</sup> In two cases IOTA failed to locate the source in the VIKING Z band because of stray light affecting the image.

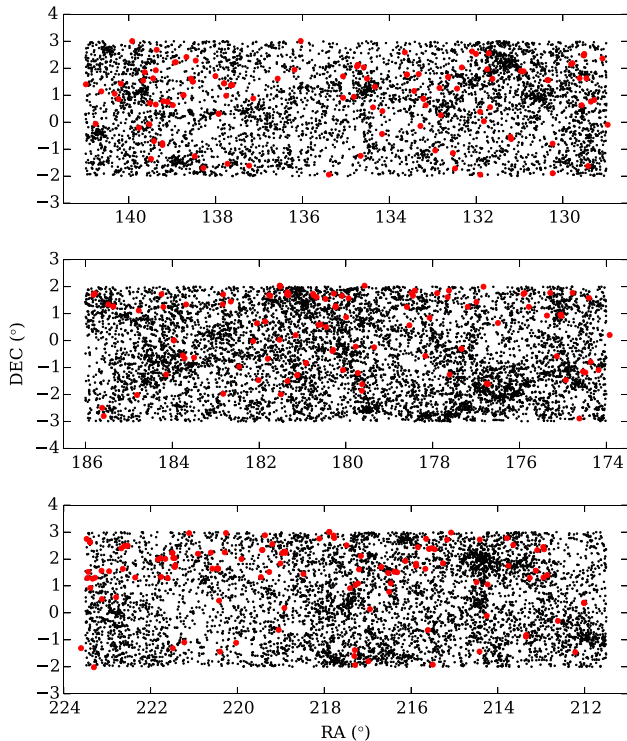


**Figure 6.** Sky positions of the 343 LSBGs across all fields, G09, G12, and G15 (top, middle, bottom, respectively; red circles). Also plotted are all confirmed galaxies in the GAMA survey which have known redshifts less than 0.1 (black points).

than 0.1 magnitudes than the fixed aperture, in which case, the fixed aperture magnitude is used. None of the  $r$ -band magnitudes were brighter than 19.8. Therefore, this LSBG sample does not have a direct effect on the calculation of the low-mass end of the GSMF using the GAMA main survey, which has an  $r < 19.8$  limit. The SB of these objects have  $\mu_r > 24.2$  mag arcsec $^{-2}$  measured within the AUTO apertures. Fig. 7 shows the distribution of SB versus magnitude for the LSBGs in comparison to GAMA samples. The photometry for the GAMA samples was also computed using IOTA with the VIKING Z band as the aperture-defining band.

### 5.3 Colour distribution

Redshifts have not yet been determined spectroscopically for these galaxies. However, the low SBs of these objects suggest that they could be low-mass galaxies and therefore at low redshift. A useful indicator of redshift can be given by a plot of  $J - K$  versus  $g - i$  colour, as shown in Baldry et al. (2010), for  $z \lesssim 0.4$  in particular. The  $g - i$  colour is sensitive to the 4000 Å break as it moves through the  $g$  band, and  $J - K$  is sensitive to the position of the ‘stellar bump’.

Fig. 8 shows the colours of the majority of the 343 sources detected with the search algorithm, as well as distributions for GAMA redshift samples with AUTO-aperture photometry (Driver et al. 2016b). These data are split into redshift bins and contoured to show where the peak density of each redshift range sits on the plot. A large proportion of the data sit around the peaks of the lower redshift bands as shown by the median value displayed in Fig. 8. There is scatter within this distribution,

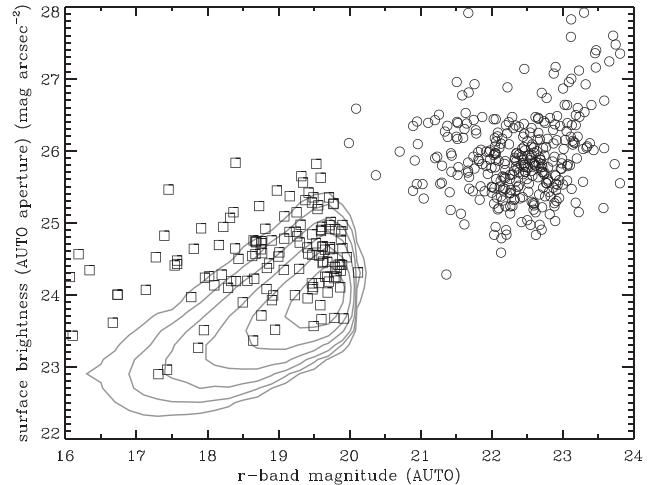


**Figure 7.**  $r$ -band SB versus magnitude for the GAMA main survey sample (contours), newly discovered LSBGs (circles) and the GAMA low-mass sample (squares), which were used to weight the images as described in Section 3. This shows how the newly discovered systems compare to the GAMA sample and show they sit outside the main survey magnitude limit. This means that they do not affect any calculation of the GSMF using an  $r < 19.8$  sample. Note that the apertures for this plot were defined using the deeper VIKING Z band, and that a Galactic-extinction correction has not been applied (sources with extinction  $a_r > 0.17$  have been excluded).

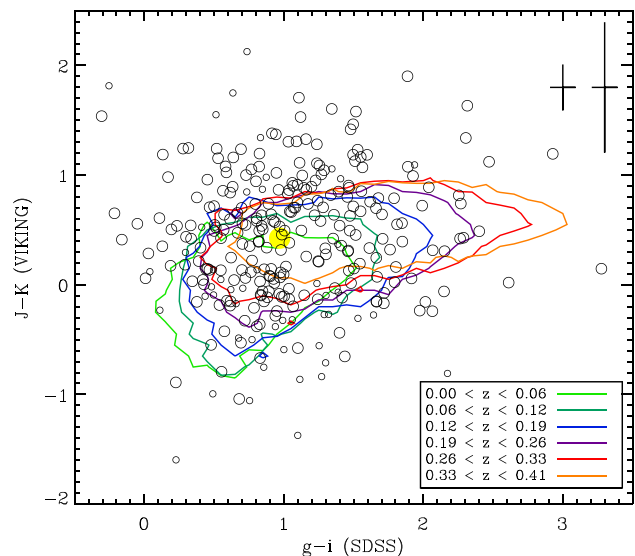


**Figure 8.** A  $g - i$  versus  $J - K$  colour-colour plot of all LSBGs (circles) found using the methods described in this paper. The contours show where the majority of galaxies in the GAMA fields lie in this space, split into redshift bins. This bivariate distribution is useful to determine if the object could be at low redshift (Baldry et al. 2010). The scatter for LSBGs was expected due to large uncertainties on the magnitudes. The median  $1\sigma$  uncertainties for the large circles and small circles are shown in the top right of the plot (LSBGs with  $1\sigma$  uncertainties larger than 1 mag are not shown). The yellow circle shows the median value of the LSBG distribution.

however; this was expected as the low-SB nature of the objects means that the uncertainties on the colours are large. Follow up is needed with spectroscopy to determine accurate redshifts of these objects.

**Table 2.** Selected detections.  $a$  and  $b$  are the semimajor and semiminor axis of the aperture fit,  $m_r$  and  $m_z$  are the  $r$ -band and  $Z$ -band apparent magnitudes of the measured objects, and  $\mu_r$  is the SB within the aperture. The magnitude uncertainties from Source Extractor are formally less than 0.1 for most of this sample; these uncertainties do not take account of possible systematic errors in the aperture or sky subtraction. Data for this sample can be obtained from the GAMA Panchromatic Swarp Imager at [gama-psi.icrar.org](http://gama-psi.icrar.org).

| ID       | RA<br>(deg) | Dec.<br>(deg) | $a$<br>(arcsec) | $b$<br>(arcsec) | $m_r$<br>(mag) | $m_z$<br>(mag) | $\mu_r$<br>(mag arcsec <sup>-2</sup> ) |
|----------|-------------|---------------|-----------------|-----------------|----------------|----------------|--|
| LSB09005 | 129.418 78  | -1.627 02     | 6.1             | 4.0             | 21.2           | 21.1           | 25.9                                   |
| LSB09006 | 129.459 62  | 1.624 07      | 5.7             | 4.9             | 21.5           | 20.6           | 26.4                                   |
| LSB09013 | 129.808 73  | 2.149 59      | 4.8             | 4.4             | 21.4           | 20.7           | 26.0                                   |
| LSB09032 | 132.438 39  | 1.243 16      | 7.2             | 5.7             | 20.7           | 20.7           | 26.0                                   |
| LSB09034 | 132.534 61  | -1.146 53     | 9.2             | 4.5             | 21.1           | 20.5           | 26.4                                   |
| LSB09035 | 132.638 10  | 1.675 91      | 5.8             | 4.6             | 23.2           | 21.2           | 28.0                                   |
| LSB09037 | 132.813 47  | 0.257 72      | 10.5            | 8.4             | 20.0           | 19.7           | 26.1                                   |
| LSB09040 | 133.161 44  | 0.626 01      | 6.8             | 3.5             | 21.7           | 20.7           | 26.4                                   |
| LSB09041 | 133.211 52  | 0.864 45      | 6.3             | 3.8             | 23.1           | 21.0           | 27.8                                   |
| LSB09042 | 133.213 06  | 0.866 27      | 6.8             | 5.3             | 21.7           | 20.4           | 26.8                                   |
| LSB09045 | 133.427 39  | 1.154 88      | 5.5             | 3.9             | 20.9           | 20.9           | 25.4                                   |
| LSB09047 | 133.598 85  | 1.761 72      | 5.7             | 3.4             | 23.1           | 20.9           | 27.6                                   |
| LSB09064 | 136.184 38  | 1.942 80      | 5.3             | 3.0             | 21.5           | 20.8           | 25.8                                   |
| LSB09078 | 138.460 61  | 2.282 20      | 5.1             | 2.8             | 22.1           | 21.6           | 26.2                                   |
| LSB09082 | 138.568 44  | 1.615 52      | 6.1             | 4.4             | 21.4           | 20.9           | 26.2                                   |
| LSB09088 | 138.987 69  | 0.630 62      | 7.9             | 6.2             | 20.9           | 20.5           | 26.4                                   |
| LSB09095 | 139.379 87  | 1.922 91      | 5.0             | 3.2             | 21.3           | 20.7           | 25.5                                   |
| LSB09110 | 140.766 13  | -0.059 94     | 4.8             | 4.1             | 21.4           | 21.4           | 25.9                                   |
| LSB09111 | 140.990 66  | 1.400 64      | 5.8             | 5.0             | 21.6           | 21.1           | 26.5                                   |
| LSB12115 | 174.401 37  | 1.579 54      | 9.2             | 5.2             | 20.9           | 20.6           | 26.3                                   |
| LSB12119 | 174.777 14  | 1.773 43      | 5.4             | 3.7             | 21.0           | 21.2           | 25.5                                   |
| LSB12133 | 176.830 34  | 1.998 69      | 11.0            | 9.1             | 21.7           | 18.9           | 27.9                                   |
| LSB12143 | 178.169 78  | -0.566 24     | 4.8             | 3.2             | 22.9           | 21.0           | 27.1                                   |
| LSB12153 | 179.633 20  | -1.857 74     | 5.1             | 4.3             | 20.9           | 20.7           | 25.5                                   |
| LSB12156 | 179.937 96  | 1.570 97      | 5.0             | 2.9             | 21.8           | 21.1           | 26.0                                   |
| LSB12159 | 180.090 84  | 1.664 13      | 6.2             | 4.8             | 21.3           | 20.5           | 26.3                                   |
| LSB12167 | 180.468 68  | 1.541 37      | 6.1             | 3.8             | 22.2           | 20.5           | 26.9                                   |
| LSB12168 | 180.582 29  | 0.596 35      | 7.3             | 3.9             | 21.5           | 20.6           | 26.4                                   |
| LSB12183 | 181.345 40  | 1.791 83      | 11.9            | 10.6            | 20.1           | 19.7           | 26.6                                   |
| LSB12187 | 181.504 72  | 2.008 95      | 4.3             | 3.8             | 22.9           | 22.0           | 27.2                                   |
| LSB12196 | 182.013 51  | -1.469 78     | 7.8             | 4.7             | 21.8           | 20.5           | 26.9                                   |
| LSB12200 | 182.653 47  | 1.447 55      | 5.5             | 3.9             | 21.6           | 21.1           | 26.2                                   |
| LSB12214 | 184.810 06  | -2.019 08     | 5.2             | 4.6             | 21.6           | 20.8           | 26.3                                   |
| LSB12218 | 185.579 48  | -2.799 34     | 7.0             | 6.9             | 21.5           | 19.8           | 27.0                                   |
| LSB12221 | 185.816 28  | 1.698 55      | 4.9             | 3.8             | 22.0           | 20.9           | 26.4                                   |
| LSB15232 | 213.262 99  | 1.298 25      | 5.2             | 3.8             | 21.3           | 20.8           | 25.8                                   |
| LSB15237 | 213.755 83  | 1.751 08      | 5.8             | 4.3             | 21.6           | 21.2           | 26.4                                   |
| LSB15239 | 214.237 05  | 1.057 52      | 5.0             | 3.9             | 21.8           | 21.1           | 26.2                                   |
| LSB15244 | 215.076 65  | 2.982 20      | 9.2             | 4.1             | 21.6           | 20.6           | 26.8                                   |
| LSB15245 | 215.168 92  | 2.718 34      | 6.3             | 3.8             | 21.5           | 20.2           | 26.2                                   |
| LSB15249 | 215.519 84  | 2.400 10      | 5.6             | 4.0             | 21.9           | 20.9           | 26.5                                   |
| LSB15250 | 215.583 28  | 2.377 87      | 8.3             | 4.4             | 21.0           | 20.7           | 26.1                                   |
| LSB15251 | 215.583 16  | 2.378 85      | 5.2             | 2.8             | 22.2           | 21.4           | 26.4                                   |
| LSB15267 | 216.686 54  | 1.699 57      | 5.3             | 4.5             | 22.5           | 20.7           | 27.1                                   |
| LSB15274 | 217.286 80  | -1.931 28     | 5.3             | 3.1             | 21.3           | 22.1           | 25.6                                   |
| LSB15280 | 217.783 22  | 2.871 96      | 5.4             | 3.8             | 21.8           | 21.1           | 26.3                                   |
| LSB15283 | 218.111 56  | 2.757 46      | 5.7             | 2.9             | 21.0           | 20.7           | 25.3                                   |
| LSB15284 | 218.479 39  | 1.444 70      | 5.1             | 4.7             | 21.2           | 20.5           | 25.9                                   |
| LSB15286 | 218.899 58  | 2.275 86      | 5.8             | 3.9             | 23.3           | 21.3           | 27.9                                   |
| LSB15297 | 219.905 55  | 1.997 90      | 6.8             | 4.5             | 20.9           | 20.9           | 25.9                                   |
| LSB15305 | 220.467 07  | 1.651 67      | 8.7             | 4.6             | 21.3           | 20.3           | 26.5                                   |
| LSB15307 | 220.612 05  | 2.238 53      | 6.5             | 4.8             | 21.4           | 20.6           | 26.3                                   |
| LSB15308 | 220.908 56  | 2.195 08      | 5.2             | 3.1             | 21.4           | 21.1           | 25.7                                   |
| LSB15326 | 222.606 28  | 2.477 10      | 8.0             | 4.9             | 21.2           | 20.4           | 26.4                                   |
| LSB15329 | 222.792 91  | 0.582 35      | 4.8             | 3.8             | 22.1           | 20.8           | 26.4                                   |
| LSB15330 | 222.954 73  | 1.546 44      | 4.8             | 4.8             | 21.5           | 21.2           | 26.2                                   |
| LSB15336 | 223.388 22  | 0.930 69      | 8.4             | 4.9             | 20.4           | 20.3           | 25.7                                   |

## 5.4 Catalogue

Analysis of the 343 detected LSBGs were presented in the previous sections. These were confirmed by deeper imaging from VISTA VIKING, which became available recently through the GAMA collaboration. To provide a sample that could be used, for example, to test how well detection and measurement codes work on LSBGs, we selected a subsample of 57. These were all the LSBGs measured with IOTA to have large angular extent,  $a > 5$  arcsec or  $ab > 15$  arcsec<sup>2</sup>, and with  $r < 23.5$ . This includes all 20 with  $r < 21.3$ . Selected data on these 57 LSBGs are given in Table 2.

## 6 SUMMARY AND CONCLUSIONS

This work attempts to answer a simple question: are there any LSBGs hidden within the GAMA equatorial regions that could contribute to the low-mass end of the GAMA GSMF? Using images from the SDSS, and a specially developed algorithm to process the images and detect the objects it was discovered that whilst there are LSBGs, they do not meet the required magnitude cut of  $r < 19.8$  mag. Therefore, they do not affect the GAMA GSMF at low masses as presented in Baldry et al. (2012). If they are low-mass galaxies, they could be significant for any attempt to measure further down the GSMF using a deeper sample such as from the Wide Area VISTA Extragalactic Survey (Driver et al. 2016a).

The algorithm created consisted of several parts: the weighting and co-adding of the images, masking, and smoothing to bring out any hidden objects within the images. A cut of  $5\sigma$  was then applied to the images to identify any pixels with a high enough SNR to be considered a detection. After clumping the detected pixels into candidate objects, a set of constraints were applied to these objects. This removed most of them as erroneous detections such as from extended wings of bright stars and galaxies that were not masked out, and from stray light from bright stars in neighbouring fields. After a final comparison to VIKING Z band, 343 new galaxy detections were confirmed.

The magnitudes and SBs of the final sample were determined primarily using an AUTO aperture. The majority of objects were consistent with being at low redshift,  $z < 0.2$ , when comparing a  $J - K$  versus  $g - i$  plot of all candidates to the GAMA main survey (Fig. 8). This plot is a good proxy for photometric redshift and can give a visual indication of whether the objects are at low or high redshift. Only a minority are likely to be in our cosmological neighbourhood within 100 Mpc, however, it should be noted that the uncertainties in the colours are probably underestimated because of the difficulty in measuring accurate photometry of LSBGs.

Fig. 7 shows how the newly discovered sample compares to the main GAMA survey in terms of SB and magnitude. It is clear that the systems discovered in this work are too faint to be included in any calculations of the GSMF using the GAMA main survey limit. However, the LSBG catalogue can be used in future studies as a test sample for deeper imaging in the same regions. Source detection software run on deeper imaging such as KiDS and VIKING should readily detect these galaxies, however, this may not be the case in reality as errors in sky subtraction and/or flat fielding can also prevent the identification of low-SB features and galaxies. In future, we plan to use a source extraction run on the VIKING Z-band mosaics matched to the GAMA redshifts to improve on estimates of the low-mass end of GSMF.

## ACKNOWLEDGEMENTS

GAMA is a joint European-Australasian project based around a spectroscopic campaign using the AAT. The GAMA input catalogue is based on data taken from the SDSS and the UKIRT Infrared Deep Sky Survey. Complementary imaging of the GAMA regions is being obtained by a number of independent survey programmes including GALEX MIS, VST KiDS, VISTA VIKING, WISE, Herschel-ATLAS, GMRT, and ASKAP providing UV to radio coverage. GAMA is funded by the STFC (UK), the ARC (Australia), the AAO, and the participating institutions. The GAMA website is <http://www.gama-survey.org/>.

## REFERENCES

- Abazajian K. N. et al., 2009, *ApJS*, 182, 543  
 Alpaslan M. et al., 2014, *MNRAS*, 438, 177  
 Bahcall N. A., 1988, *ARA&A*, 26, 631  
 Baldry I. K., Glazebrook K., Driver S. P., 2008, *MNRAS*, 388, 945  
 Baldry I. K. et al., 2010, *MNRAS*, 404, 86  
 Baldry I. K. et al., 2012, *MNRAS*, 421, 621  
 Bell E. F., McIntosh D. H., Katz N., Weinberg M. D., 2003, *ApJS*, 149, 289  
 Belokurov V. et al., 2010, *ApJ*, 712, L103  
 Benson A. J., Frenk C. S., Lacey C. G., Baugh C. M., Cole S., 2002, *MNRAS*, 333, 177  
 Bertin E., Arnouts S., 1996, *A&AS*, 117, 393  
 Binggeli B., Sandage A., Tammann G. A., 1988, *ARA&A*, 26, 509  
 Blanton M. R., Lupton R. H., Schlegel D. J., Strauss M. A., Brinkmann J., Fukugita M., Loveday J., 2005, *ApJ*, 631, 208  
 Cross N., Driver S. P., 2002, *MNRAS*, 329, 579  
 de Vaucouleurs G., 1959, *Handbuch Phys.*, 53, 275  
 de Vaucouleurs G., Ables H. D., 1968, *ApJ*, 151, 105  
 Davies J. I., Davies L. J. M., Keenan O. C., 2016, *MNRAS*, 456, 1607  
 Disney M. J., 1976, *Nature*, 263, 573  
 Disney M., Phillipps S., 1983, *MNRAS*, 205, 1253  
 Driver S. P., Liske J., Cross N. J. G., De Propriis R., Allen P. D., 2005, *MNRAS*, 360, 81  
 Driver S. P. et al., 2009, *Astron. Geophys.*, 50, 5.12  
 Driver S. P. et al., 2011, *MNRAS*, 413, 971  
 Driver S. P. et al., 2012, *MNRAS*, 427, 3244  
 Driver S. P., Davies L. J., Meyer M., Power C., Robotham A. S. G., Baldry I. K., Liske J., Norberg P., 2016a, in Napolitano N. R., Longo G., Marconi M., Paolillo M., Iodice E., eds, *Astrophys. Space Sci. Proc. Vol. 42, The Universe of Digital Sky Surveys*. Springer-Verlag, Berlin, p. 205  
 Driver S. P. et al., 2016b, *MNRAS*, 455, 3911  
 Du W., Wu H., Lam M. I., Zhu Y., Lei F., Zhou Z., 2015, *AJ*, 149, 199  
 Edge A., Sutherland W., Kuijken K., Driver S., McMahon R., Eales S., Emerson J. P., 2013, *The Messenger*, 154, 32  
 Emerson J., Sutherland W., 2010, *The Messenger*, 139, 2  
 Ferrara A., Tolstoy E., 2000, *MNRAS*, 313, 291  
 Fliri J., Trujillo I., 2016, *MNRAS*, 456, 1359  
 Fukugita M., Ichikawa T., Gunn J. E., Doi M., Shimasaku K., Schneider D. P., 1996, *AJ*, 111, 1748  
 Geha M., Blanton M. R., Yan R., Tinker J. L., 2012, *ApJ*, 757, 85  
 Geller M. J., Diaferio A., Kurtz M. J., Dell'Antonio I. P., Fabricant D. G., 2012, *AJ*, 143, 102  
 Gilmore G., Wilkinson M. I., Wyse R. F. G., Kleya J. T., Koch A., Evans N. W., Grebel E. K., 2007, *ApJ*, 663, 948  
 Giovanelli R. et al., 2005, *AJ*, 130, 2598  
 Giovanelli R. et al., 2013, *AJ*, 146, 15  
 Guo Q. et al., 2011, *MNRAS*, 413, 101  
 Hoefl M., Yepes G., Gottlöber S., Springel V., 2006, *MNRAS*, 371, 401  
 Hopkins A. M. et al., 2013, *MNRAS*, 430, 2047  
 Huang S., Haynes M. P., Giovanelli R., Brinchmann J., 2012, *ApJ*, 756, 113  
 Hubble E. P., 1926, *ApJ*, 64, 321  
 Ibata R., Martin N. F., Irwin M., Chapman S., Ferguson A. M. N., Lewis G. F., McConnachie A. W., 2007, *ApJ*, 671, 1591

- Impey C., Bothun G., 1997, *ARA&A*, 35, 267
- Impey C. D., Sprayberry D., Irwin M. J., Bothun G. D., 1996, *ApJS*, 105, 209
- Irwin M. J. et al., 2007, *ApJ*, 656, L13
- James B. L., Kaposov S., Stark D. P., Belokurov V., Pettini M., Olszewski E. W., 2015, *MNRAS*, 448, 2687
- Janz J. et al., 2016, *MNRAS*, 456, 617
- Jennings Z. G. et al., 2015, *ApJ*, 812, L10
- Kang X., Macciò A. V., Dutton A. A., 2013, *ApJ*, 767, 22
- Karachentsev I. D., Karachentseva V. E., Huchtmeier W. K., Makarov D. I., 2004, *AJ*, 127, 2031
- Kelvin L. S. et al., 2014a, *MNRAS*, 439, 1245
- Kelvin L. S. et al., 2014b, *MNRAS*, 444, 1647
- Kissler-Patig M., 2004, in Lamers H. J. G. L. M., Smith L. J., Nota A., eds, *ASP Conf. Ser. Vol. 322, The Formation and Evolution of Massive Young Star Clusters*. Astron. Soc. Pac., San Francisco, p. 535
- Klypin A., Kravtsov A. V., Valenzuela O., Prada F., 1999, *ApJ*, 522, 82
- Kniazev A. Y., Grebel E. K., Pustilnik S. A., Pramskij A. G., Kniazeva T. F., Prada F., Harbeck D., 2004, *AJ*, 127, 704
- Koposov S. et al., 2008, *ApJ*, 686, 279
- Kormendy J., 1985, *ApJ*, 295, 73
- Kuijken K., 2011, *The Messenger*, 146, 8
- Lapi A., Danese L., 2015, *J. Cosmol. Astropart. Phys.*, 9, 3
- Liske J. et al., 2015, *MNRAS*, 452, 2087
- McConnachie A. W., 2012, *AJ*, 144, 4
- McGaugh S. S., 1996, *MNRAS*, 280, 337
- Mahajan S. et al., 2015, *MNRAS*, 446, 2967
- Martin N. F. et al., 2009, *ApJ*, 705, 758
- Martin N. F., Slater C. T., Schlafly E. F., Morganson E., Rix H.-W., 2013, *ApJ*, 772, 15
- Miskolczi A., Bomans D. J., Dettmar R.-J., 2011, *A&A*, 536, A66
- Moore B., Ghigna S., Governato F., Lake G., Quinn T., Stadel J., Tozzi P., 1999, *ApJ*, 524, L19
- Muzzin A. et al., 2013, *ApJ*, 777, 18
- Peebles P. J. E., 2001, *ApJ*, 557, 495
- Peek J. E. G. et al., 2011, *ApJS*, 194, 20
- Phillipps S., Drinkwater M. J., Gregg M. D., Jones J. B., 2001, *ApJ*, 560, 201
- Press W. H., Schechter P., 1974, *ApJ*, 187, 425
- Richardson J. C. et al., 2011, *ApJ*, 732, 76
- Rosenbaum S. D., Krusch E., Bomans D. J., Dettmar R.-J., 2009, *A&A*, 504, 807
- Sand D. J. et al., 2015, *ApJ*, 806, 95
- Scaramella R., Sabatini S., 2009, *Mem. Soc. Astron. Ital. Suppl.*, 13, 142
- Shapley H., 1938, *Nature*, 142, 715
- Sharp R. et al., 2006, in McLean I. S., Iye M., eds, *Proc. SPIE Conf. Ser. Vol. 6269, Ground-based and Airborne Instrumentation for Astronomy*. SPIE, Bellingham, p. 62690G
- Somerville R. S., 2002, *ApJ*, 572, L23
- Stoughton C. et al., 2002, *AJ*, 123, 485
- Taylor E. N. et al., 2011, *MNRAS*, 418, 1587
- Tollerud E. J., Geha M. C., Grcevich J., Putman M. E., Stern D., 2015, *ApJ*, 798, L21
- Trachternach C., Bomans D. J., Habertzell L., Dettmar R.-J., 2006, *A&A*, 458, 341
- van Dokkum P. G., Abraham R., Merritt A., Zhang J., Geha M., Conroy C., 2015, *ApJ*, 798, L45
- Walsh S. M., Jerjen H., Willman B., 2007, *ApJ*, 662, L83
- Walsh S. M., Willman B., Jerjen H., 2009, *AJ*, 137, 450
- York D. G. et al., 2000, *AJ*, 120, 1579
- Zwicky F., Zwicky M. A., 1971, *Catalogue of Selected Compact Galaxies and of Post-eruptive Galaxies*. F. Zwicky, Guemligen, Switzerland

This paper has been typeset from a  $\text{\TeX}/\text{\LaTeX}$  file prepared by the author.